Available online at www.sciencedirect.com
SCIENCE DIRECT®
Comput. Methods Appl. Mech. Engrg. 194 (2005) 4565–4587
Computer methods in applied mechanics and engineering
www.elsevier.com/locate/cma

Computation of incompressible bubble dynamics with a stabilized finite element level set method

Sunitha Nagrath [a,b], Kenneth E. Jansen [a,b,*], Richard T. Lahey Jr. [b]

[a] *Scientific Computation Research Center, Rensselaer Polytechnic Institute, Troy, NY 12180-3590, USA*
[b] *Department of Mechanical, Aeronautical and Nuclear Engineering, Rensselaer Polytechnic Institute, Troy, NY 12180-3590, USA*

Received 17 October 2003; received in revised form 8 November 2004; accepted 23 November 2004

Abstract

This paper presents a stabilized finite element method for the three dimensional computation of incompressible bubble dynamics using a level set method. The interface between the two phases is resolved using the level set approach developed by Sethian [Level Set Methods and Fast Marching Methods, Cambridge University Press, 1999], Sussman et al. [J. Comput. Phys. 114 (1994) 146], and Sussman et al. [J. Comput. Phys. 148 (1999) 81–124]. In this approach the interface is represented as a zero level set of a smooth function. The streamline-upwind/Petrov–Galerkin method was used to discretize the governing flow and level set equations. The continuum surface force (CSF) model proposed by Brackbill et al. [J. Comput. Phys. 100 (1992) 335–354] was applied in order to account for surface tension effects. To restrict the interface from moving while re-distancing, an improved re-distancing scheme proposed in the finite difference context [J. Comput. Phys. 148 (1999) 81–124] is adapted for finite element discretization. This enables us to accurately compute the flows with large density and viscosity differences, as well as surface tension. The capability of the resultant algorithm is demonstrated with two and three dimensional numerical examples of a single bubble rising through a quiescent liquid, and two bubble coalescence.

Keywords: Finite element; Level set; SUPG; Two phase incompressible flow; Bubble dynamics

* Corresponding author. Address: Department of Mechanical, Aeronautical and Nuclear Engineering, Rensselaer Polytechnic Institute, Troy, NY 12180-3590, USA. Tel.: +1 518 276 6755; fax: +1 518 276 6025.
E-mail addresses: nagras@scorec.rpi.edu (S. Nagrath), kjansen@scorec.rpi.edu (K.E. Jansen), laheyr@rpi.edu (R.T. Lahey Jr.).

0045-7825/$ - see front matter © 2005 Elsevier B.V. All rights reserved.
doi:10.1016/j.cma.2004.11.012

1. Introduction

The development of efficient algorithms to understand the hydrodynamics of multi-phase flow systems is one of the most pressing engineering challenges facing chemical, petrochemical, nuclear, combustion and biological industries today. Owing to the advances in numerical methods and as well as in computational hardware performance, numerical experiments have become increasingly popular in the study of complex multi-fluid systems. There are various numerical methods that are available in literature to compute multi-phase flows. They are often used to understand fundamental processes involving bubble dynamics. In the study of bubble dynamics, the understanding of the behavior of a bubble rising through a liquid is an important problem. Indeed this important two-phase flow phenomena has been extensively studied.

The buoyancy driven motion of a bubble in a viscous liquid is normally accompanied by the deformation of the bubble. Three dimensional studies of this phenomena become complex due to the effect of free boundaries, significant density and viscosity differences and the effect of surface tension. Various experimental studies have been performed to address this problem. Observations by Hartunian and Sears [5], Walters and Davidson [6], Grace [7], and Bhaga and Weber [8] are important experimental studies in literature. Similarly, there exists various numerical techniques. Existing computational methods used to solve multiphase flow problems, have their own advantages and disadvantages. In all multiphase numerical methods, the essential ingredients are an efficient technique to solve the phasic flow fields, and an accurate strategy to keep track of the interface. Various techniques are available for solving the governing partial differential equations (PDEs) of basic flow, namely Finite Difference methods (FDM), Finite Volume methods (FVM), and Finite Element methods (FEM). We have chosen the finite element method for it's ease of treatment of complex geometries. Also the method can be readily improved to perform efficient computations with adaptive remeshing.

Over the last several decades, finite element methods have grown in popularity; particularly stabilized finite element methods are vastly applied for fluid dynamics applications. Starting with the SUPG method of Brooks and Hughes [9] through the work of Hughes et al. [10] on the Galerkin/least squares (GLS) method and up to recent work on multi-scale methods of Hughes [11] and the related work on residual-free bubbles by Russo [12] and Brezzi et al. [13], a number of stabilized FEM formulations have been proposed. A key feature of stabilized methods is that they have been proven to be stable and to attain optimal convergence rates with respect to the interpolation error (e.g, see Franca and Frey [14], and Hughes et al. [10]). In the present work, a stabilized finite element method is employed for computing both flow, and interface motion.

In multi-phase flow simulations, when it comes to the resolving of interface motion, two types of methods are employed, namely, interface tracking, or interface capturing methods [15]. The interface/front tracking techniques use a deforming mesh or grid which conforms to the interface, or explicitly tracks the interface (e.g. marker particles). Examples are front tracking methods [16], boundary integral methods [17], arbitrary Lagrangian–Eulerian (ALE) methods [18], and deforming space-time finite element formulations [19,20]. An advantage of front tracking methods is that they are accurate with comparatively lower mesh resolution. Also, they are efficient for rigid moving boundaries. However, the algorithms have to be modified to reconnect, or disconnect the interfaces separating the various fluids. In addition, significant remeshing is needed to prevent the so-called marker particles (which track the interface) from coming together at points of large curvature. On the other hand, in interface capturing methods, an auxiliary function defined on the fixed domain describes the interface. The interface capturing methods are very robust with wide range of applicability, however they require higher mesh resolution. Examples are volume of fluid methods (VOF) [21], phase field methods, front capturing methods, and level set methods [1–3]. Volume of fluid methods are based on solving the conservation law for the volume fraction and they have excellent conservation properties within each phase. However, in VOF method it is difficult to calculate the curvature

of the interface from the computed volume fractions. Although the level set method does not possess the same inherent conservation properties as volume of fluid methods or front tracking techniques, the strength of this method lies in it's ability to efficiently represent an arbitrarily complex interface very accurately, thereby allowing the computation of flows with surface tension and rapidly changing topology.

In the literature, Li et al. [22] studied the deformation of the three dimensional bubble using a modified VOF method with finite difference discretization. Sussman et al. [2] presented a level set approach to study the same problem, again using a finite difference approximation. Barth and Sethian [23] developed a finite element Petrov–Galerkin scheme for the level set equations on triangulated domains. The present work extends the aforementioned works to present a stabilized three dimensional, finite element approach using the level set method for solving two-phase incompressible bubbly flows.

The outline of this paper is as follows. We first present the governing equations in Section 2. Then we introduce the level set method. Section 3 describes the finite element formulations for solving the incompressible equations of motion, which are discretized in space using a stabilized finite element method to obtain a nonlinear system of coupled ordinary differential equations. Additionally, in this section we present the finite element solution technique for solving both the level set and the re-distancing equations, which also includes a strategy to restrict the interface from moving during re-distancing. Section 4 presents the results and discussion and Section 5 presents conclusions and suggestions for future work.

2. Governing equations

When both phases of the flow can be considered incompressible, and as well as immiscible, the governing equations for the flow are the well known equations of motion represented as (see [24] for more detail on notation):

$$\rho(\dot{u}_i + u_j u_{i,j}) = -p_{,i} + \tau_{ij,j} + f_i, \tag{1}$$

$$u_{i,i} = 0. \tag{2}$$

The density and the viscosity are simply convected by the fluid velocity. The variables are: the velocity u_i, the pressure p, the density ρ. Constitutive laws relate the stress tensor, τ_{ij}, to the deviatoric portion of the strain, $S^d_{ij} = S_{ij} - \frac{1}{3}S_{kk}\delta_{ij}$, through a molecular viscosity, μ. For an incompressible flow, from (2) the divergence of the flow is zero, hence the stress tensor is simply the symmetric strain rate tensor. Hence

$$\tau_{ij} = \mu(u_{i,j} + u_{j,i}). \tag{3}$$

Finally f is a volumetric source term, such as gravity and the interfacial force resulting from the surface tension. The representation of the surface tension surface force as a body force applied on the interface is dealt with in Section 2.2 in detail. Density and viscosity are considered constant along the stream lines. Further, we assume that the density and viscosity are constant in each phase and they vary only across the interface. Hence, their variation could be governed by a single smooth function, namely the level set function, which is discussed in detail in Section 2.1.

2.1. The level set method

The level set approach represents the free surface as a zero level set of a smooth function, and simultaneously maintains a level set function, which by definition is the signed distance from the interface. Hence, instead of explicitly tracking the interface, we implicitly "capture" the interface within a field which is interpolated with finite element basis functions like any other state variable (e.g, pressure, velocity, temperature). As mentioned in [2], conventional conservative methods suffer with excessive numerical diffusion which

smears the sharpness of the front. The level set function is typically a smooth (Lipschitz continuous) function, denoted here as ϕ, which eliminates the difficulties that conventional conservative schemes incur.

Probably the most important advantage of level set methods is that the interfaces can merge or break-up with ease. Furthermore, the level set formulation generalizes easily to three dimensions. The actual location of the interface is never computed, since the interface is embedded as a particular level set in a fixed domain.

In our formulations, a smooth level set function, ϕ, is used to track the interface between the gas phase and the liquid phase. The interface, Γ', is the zero level set of ϕ:

$$\Gamma' = \{\boldsymbol{x} | \phi(\boldsymbol{x}, t) = 0\}. \tag{4}$$

The level set function is considered to be positive in the liquid phase and negative in the gas phase. Hence we have,

$$\phi(\boldsymbol{x}, t) = \left\{ \begin{array}{ll} > 0 & \text{if } \boldsymbol{x} \in \text{the liquid} \\ = 0 & \text{if } \boldsymbol{x} \in \Gamma' \\ < 0 & \text{if } \boldsymbol{x} \in \text{the gas} \end{array} \right\}. \tag{5}$$

Therefore, we initialize ϕ to be the signed normal distance from the interface. Since the interface moves with the fluid, the evolution of ϕ is governed by a transport equation:

$$\phi_{,t} + u_i \phi_{,i} = 0. \tag{6}$$

As discussed in Section 3.1, this additional advection equation for the level set scalar is solved in a manner similar to the equations of motion. The physical properties of the fluid in each phase are calculated as a function of ϕ as:

$$\rho(\phi) = \rho_1 H(\phi) + \rho_2 (1 - H(\phi)), \tag{7}$$

and similarly,

$$\mu(\phi) = \mu_1 H(\phi) + \mu_2 (1 - H(\phi)), \tag{8}$$

where $H(\phi)$ is the Heaviside function given by

$$H(\phi) = \left\{ \begin{array}{ll} 0 & \text{if } \phi < 0 \\ \dfrac{1}{2} & \text{if } \phi = 0 \\ 1 & \text{if } \phi > 0 \end{array} \right\}. \tag{9}$$

2.1.1. Interface thickness

Use of the Heaviside function described above leads to poor results due to the assumed zero thickness of the interface. Instead, we can use an alternative description of the interface as proposed by [2,16,3]. Numerically, they substitute a smoothed Heaviside function $H_\epsilon(\phi)$ for the sharp Heaviside function $H(\phi)$. The smooth Heaviside function is defined as [3]:

$$H_\epsilon(\phi) = \left\{ \begin{array}{ll} 0 & \text{if } \phi < -\epsilon \\ \dfrac{1}{2}\left[1 + \dfrac{\phi}{\epsilon} + \dfrac{1}{\pi} \sin\left(\dfrac{\pi\phi}{\epsilon}\right)\right] & \text{if } |\phi| \leqslant \epsilon \\ 1 & \text{if } \phi > \epsilon \end{array} \right\}, \tag{10}$$

where ϕ represents the signed normal distance to the interface. The $\frac{1}{2}$ contour of the sharp Heaviside function $H(\phi)$ creates jagged or staircase contours on any discrete mesh of spacing Δx. However, by giving the interface a thickness of $\epsilon = \alpha \Delta x$, where $\alpha > 1$, sharp changes across the interface are smoothed.

2.1.2. Re-initialization or re-distancing of level sets

In the formulation describe above, the interface will have a uniform thickness so long as ϕ is maintained as a distance function. However, under the evolution of Eq. (6), the level sets that are adjacent to the zero level set may move with velocities different than that of the zero level set. Therefore, the ϕ distance field gets distorted. Thus, one must re-initialize the level set function on regular intervals in order to rebuild/maintain the signed distance function. There are several ways to accomplish this re-distancing. We have followed the technique introduced by Sussman et al. [2]. Its virtue is that the level set function can be re-initialized without explicitly finding the zero level set. The idea is to solve the partial differential equation

$$\frac{\partial d}{\partial \tau^d} = S(\phi)(1 - |d_{,i}|), \tag{11}$$

where

$$S(\phi) = \left\{ \begin{array}{ll} -1 & \text{if } \phi < 0 \\ 0 & \text{if } \phi = 0 \\ 1 & \text{if } \phi > 0 \end{array} \right\}, \tag{12}$$

$d(\boldsymbol{x}, 0) = \phi(\boldsymbol{x}, t)$ and τ^d is a pseudo time. Given any initial data for ϕ, solving this equation to steady state provides the distance field ϕ with the property $|\nabla\phi| = 1$, since convergence occurs when the right hand side of (11) is zero. Note that the sign function $S(\phi)$ controls the flow of information. If ϕ is negative, information flows one way, and if ϕ is positive, information flows the other way. The net effect is to re-distance the level sets on either side of the zero level set. Furthermore, instead of the sharp sign function we use the smooth sign function defined as

$$S(\phi) = 2(H_\epsilon(\phi) - 1/2). \tag{13}$$

The steady solutions of (11) are distance functions. In addition, since $S(0) = 0$, then $d(\boldsymbol{x}, \tau^d)$ has the same zero level set as $\phi(\boldsymbol{x}, t)$. Note, that this equation is relaxed in pseudo-time τ^d which is not related to the physical time t. Hence we only need to solve (11) for $\tau^d = 0 \cdots \epsilon \times \boldsymbol{v}$, because the level set function re-initialization is required only near the interface. The definition of the $\boldsymbol{v}$ is obvious if we re-write the (11) as

$$\frac{\partial d}{\partial \tau^d} + v_i d_{,i} = S(\phi), \tag{14}$$

where

$$v_i = S(\phi)\frac{d_{,i}}{|d_{,i}|}. \tag{15}$$

Eq. (14) is a non-linear hyperbolic equation with the characteristics pointing away from the interface in the direction of the normals (both directions). The strategy, which was adopted in the present study was to perform this re-distancing operation at the end of each time step.

2.2. Modeling of surface tension

For many fluid flow problems, interfacial motion induced by surface tension may play a significant role. The surfaces tension force is a result of the uneven molecular forces of attraction experienced by fluid molecules near the interface. Surface tension creates a microscopic, localized surface force that exerts itself in both tangential and normal directions. We use the continuum approach proposed by Brackbill et al. [4] in order to represent the surface tension force as a body force. This model represents surface tension as a continuous three dimensional effect across an interface, rather than as a boundary value condition at the interface. The resulting body force due to surface tension can be written as

$$f = -\frac{\kappa(\phi)\nabla H_\epsilon(\phi)}{W}, \tag{16}$$

where $\kappa(\phi)$ is the curvature defined as

$$\kappa(\phi) = \nabla \cdot \left(\frac{\nabla\phi}{|\nabla\phi|}\right) \tag{17}$$

and W is the Weber number given by

$$W = \frac{\rho_1 L U^2}{\sigma}. \tag{18}$$

The surface tension term and local inter-facial curvature are easily represented in terms of the level set function. As the level set function in our formulations is a signed distance from the interface, the curvature can be accurately computed from the level set function. However, the calculation of curvature involves the second order derivatives. Since we are using piecewise-linear basis functions, these second derivatives are zero on the element interior. Hence, the piecewise-constant gradients are reconstructed to be continuous using L_2 projection, and then the second order derivatives are evaluated by differentiating the reconstructed gradient. This procedure is described in detail by Jansen et al. [25]. The form of the surface tension force as a body force used here is due to Chang et al. [26].

3. Finite element discretization of the incompressible equations of motion

To derive the finite element discretization of the weak form of the equations of motion (1) and (2), we first introduce the discrete weight and solution function spaces. Let $\overline{\Omega} \subset \mathbf{R}^N$ represent the closure of the physical spatial domain (i.e. $\Omega \cup \Gamma$ where Γ is the boundary) in N dimensions; where only $N = 3$ is considered here. The boundary is decomposed into portions with natural boundary conditions, Γ_h, and essential boundary conditions, Γ_g, i.e., $\Gamma = \Gamma_g \cup \Gamma_h$. In addition, $H^1(\Omega)$ represents the usual Sobolev space of functions with square-integrable values and derivatives on Ω.

Subsequently Ω is discretized into n_{el} finite elements, $\overline{\Omega}_e$. With this, we can define the discrete trial solution and weight spaces for the semi-discrete formulation as:

$$\mathscr{S}_h^k = \{\boldsymbol{v} | \boldsymbol{v}(\cdot,t) \in H^1(\Omega)^N, t \in [0,T], \boldsymbol{v}|_{x\in\overline{\Omega}_e} \in P_k(\overline{\Omega}_e)^N, \boldsymbol{v}(\cdot,t) = \boldsymbol{g} \text{ on } \Gamma_g\}, \tag{19}$$

$$\mathscr{W}_h^k = \{\boldsymbol{w} | \boldsymbol{w}(\cdot,t) \in H^1(\Omega)^N, t \in [0,T], \boldsymbol{w}|_{x\in\overline{\Omega}_e} \in P_k(\overline{\Omega}_e)^N, \boldsymbol{w}(\cdot,t) = \boldsymbol{0} \text{ on } \Gamma_g\}, \tag{20}$$

$$\mathscr{P}_h^k = \{p | p(\cdot,t) \in H^1(\Omega), t \in [0,T], p|_{x\in\overline{\Omega}_e} \in P_k(\overline{\Omega}_e)\}, \tag{21}$$

where $P_k(\overline{\Omega}_e)$ is the space of all polynomials defined on Ω^e, complete to order $k \geqslant 1$. Let us emphasize that the local approximation space, $P_k(\overline{\Omega}_e)$, is same for both the velocity and pressure variables. This is possible due to the stabilized nature of the formulation to be introduced below. These spaces represent discrete subspaces of the spaces in which the weak form is defined.

The stabilized formulation used in the present work is based on the formulation described by Taylor et al. [27]. Given the spaces defined above, we first present the semi-discrete Galerkin finite element formulation applied to the weak form of (1) as:

Find $\boldsymbol{u} \in \mathscr{S}_h^k$ and $p \in \mathscr{P}_h^k$ such that

$$B_G(w_i, q; u_i, p) = 0, \tag{22}$$

$$B_G(w_i, q; u_i, p) = \int_\Omega \{w_i(\dot{u}_i + u_j u_{i,j} - f_i) + w_{i,j}(-p\delta_{ij} + \tau_{ij}) - q_{,i}u_i\}\,\mathrm{d}x + \int_{\Gamma_h} \{w_i(p\delta_{\mathrm{in}} - \tau_{\mathrm{in}}) + qu_n\}\,\mathrm{d}s \tag{23}$$

for all $\boldsymbol{w} \in \mathscr{W}_h^k$ and $q \in \mathscr{P}_h^k$. The boundary integral term arises from the integration by parts and is only carried out over the portion of the domain without essential boundary conditions.

Since the Galerkin method is unstable for the equal-order interpolations given above, we add additional stabilization terms: Find $\boldsymbol{u} \in \mathscr{S}_h^k$ and $p \in \mathscr{P}_h^k$ such that,

$$B(w_i, q; u_i, p) = 0, \tag{24}$$

$$B(w_i, q; u_i, p) = B_G(w_i, q; u_i, p) + \sum_{e=1}^{n_{el}} \int_{\overline{\Omega}_e} \{\tau_M(u_j w_{i,j} + q_{,i})\mathscr{L}_i + \tau_C w_{i,i} u_{j,j}\}\,\mathrm{d}x + \sum_{e=1}^{n_{el}} \int_{\overline{\Omega}_e} \{\overset{\Delta}{w_i} u_j u_{i,j} + \overset{\Delta}{\tau} u_j w_{i,j} \overset{\Delta}{u_k} u_{i,k}\}\,\mathrm{d}x \tag{25}$$

for all $\boldsymbol{w} \in \mathscr{W}_h^k$ and $q \in \mathscr{P}_h^k$. For simplicity, we have used $\mathscr{L}_i$ to represent the residual of the ith momentum equation,

$$\mathscr{L}_i = \dot{u}_i + u_j u_{i,j} + p_{,i} - \tau_{ij,j} - f_i. \tag{26}$$

The second line in the stabilized formulation, (25), represents the typical stabilization added to the Galerkin formulation for the incompressible set of equations (e.g. Franca and Frey [14]). The description of the individual terms and the stabilization parameters for continuity and momentum are discussed in detail by Whiting and Jansen [24]. The same reference also provides the remaining flow discretization details.

3.1. Finite element formulation for the level set method

Eqs. (6) and (11) can be represented by a single scalar advection equation of the form

$$\theta_{,t} + a_i \theta_{,i} = S. \tag{27}$$

In case of the level set equation, $\theta = \phi$, $\boldsymbol{a} = \boldsymbol{u}$ and the forcing function S is zero. On the other hand, in the case of re-distancing equation, $\theta = d$, $\boldsymbol{a} = \boldsymbol{v}$, and S is given by (13). This section presents the general finite element formulation for the scalar advection equation, (27). The solution strategy for solving this equation is similar to that used for the equations of motion, as discussed in Section 3.

Again, the spatial discretization is performed using the finite element method, and the finite element approximation spaces, namely the solution and the weight function space, are as defined in Section 3. In keeping with the approach of the finite element method described above, we write (6) in the residual form. To derive the weak form of residual form, (6) is multiplied by a smooth weighting function ψ belonging to a space of functions $\psi \in \Psi_h$ (the scalar counterpart of the vector space defined in Section 3). The product is then integrated over a spatial domain. As the equation is solved in the convective form, we do not integrate by parts thus there are no boundary integrals. The resulting weak form is: find $\theta \in \Theta_h$ (the scalar solution space) such that,

$$\int_\Omega (\psi\theta_{,t} + \psi a_i \theta_{,i} - \psi S)\,\mathrm{d}\Omega + \sum_{e=1}^{n_{el}} \int_{\overline{\Omega}_e} \{\widehat{\mathscr{L}}^{\mathrm{T}} \psi\tau(\theta_{,t} + a_i\theta_{,i} - S)\}\,\mathrm{d}x = 0 \tag{28}$$

for all $\psi \in \Psi_h$. Here τ is the stabilization parameter defined as

$$\tau = \frac{C}{\sqrt{c_1/\Delta t^2 + c_2 u_i g_{ij} u_j}}, \tag{29}$$

where C, c_1, and c_2 are defined based on the one-dimensional, linear advection-diffusion equation using a linear finite element basis and $g_{ij} = \xi_{k,i}\xi_{k,j}$ is the covariant metric tensor related to the mapping from global to element coordinates. Note that by replacing $\widehat{\mathscr{L}}^{\mathrm{T}}$ by $\widehat{\mathscr{L}}^{\mathrm{adv}}$ (for the scalar equation $\widehat{\mathscr{L}}^{\mathrm{adv}} = a_i \frac{\partial}{\partial x_i}$), we obtain the SUPG (Streamline Upwind Petrov–Galerkin) stabilization [9]. Next, the weight functions (ψ), the solution variable (θ), and it's time derivative ($\theta_{,t}$) are expanded in terms of linear basis functions. The integrals are then evaluated using Gauss quadrature resulting in a system of ordinary differential equations which can be written as

$$\boldsymbol{M}\dot{\theta} = \boldsymbol{N}(\theta). \tag{30}$$

The system of ODE's (linear, when $\theta = \phi$, and non-linear when $\theta = d$) is converted to an algebraic system by introducing a time integrator (generalized alpha for $\theta = \phi$, and backward Euler for $\theta = d$). Then, the two coupled systems (flow and scalar) are iterated in a staggered manner until convergence is achieved. The algorithm can be described as follows:

Staggered flow-level set solution:

- Three discrete equations
  - Flow equations (25)
  - Scalar advection equation (28)
  - Scalar advection equation with forcing function to restore distance field (28)

loop over the number of time steps
  loop over the nonlinear iteration loop
    solve flow equations
    advance the level sets
  end of the loop over nonlinear iterations
  relax the distance field
end of the loop over time steps

3.1.1. Redistancing—volume constraint

During the above described staggered iteration of solving flow equations and level set equation, the interface is convected with the local flow speed, which, as mentioned before distorts the distance function. As discussed earlier, this distance function is restored by the solution of (14) via a finite element discretization as discussed in Section 3.1. During this re-distancing step, additional care is taken to restrict the interface from moving. To constrain the interface, we implemented the strategy proposed by Sussman et al. [2] for the finite difference method. The principle behind the constraint calculations is to enforce the volume occupied by each phase in an element to remain constant, when the re-distance step is applied. The volume in each element can be defined as

$$V^k = \int_{\Omega^e} H(d^k)\,\mathrm{d}\Omega^e, \tag{31}$$

where H is the Heaviside function as given by (9), and d^k is the distance field at the kth iteration of redistancing in pseudo time, that is at τ^k. Since, we want to impose the constraint that the volume should not change, we should have $V^k = V^0$. In other words we can write

$$V^k - V^0 \approx (\tau^k - \tau^0) \int_{\Omega^e} \frac{\mathrm{d}H'_\epsilon(d^0)}{\mathrm{d}\tau}\,\mathrm{d}\Omega^e \approx \int_{\Omega^e} H'_\epsilon(d^0)(d^d - d^0)\,\mathrm{d}\Omega^e = 0, \tag{32}$$

where,

$$H'_\epsilon(d) = \begin{Bmatrix} 0 & \text{if } |d| > \epsilon \\ \frac{1}{2}\left[\frac{1}{\epsilon} + \frac{1}{\epsilon}\cos\left(\frac{\pi d}{\epsilon}\right)\right] & \text{if } |d| \leqslant \epsilon \end{Bmatrix}. \tag{33}$$

Hence, to minimize the volume variation, the current values of the level set function, denoted as $\tilde{d}^k$, are projected onto new values, denoted by d^k, which satisfy:

$$\int_{\Omega^e} H'_\epsilon(d^0)(d^k - d^0)\,\mathrm{d}\Omega^e = 0. \tag{34}$$

It is assumed that the new distance field d^k has the form,

$$d^k = \tilde{d}^k + \lambda_{\Omega^e}(\tau^k - \tau^0)H'_\epsilon(d^0), \tag{35}$$

where λ_{Ω^e} is assumed to be constant in Ω^e, and is given by,

$$\lambda_{\Omega^e} = \frac{-\int_{\Omega^e} H'_\epsilon(d^0)\left(\frac{\tilde{d}^k - d^0}{\tau^k - \tau^0}\right)\mathrm{d}\Omega^e}{\int_{\Omega^e} (H'_\epsilon(d^0))^2\,\mathrm{d}\Omega^e}. \tag{36}$$

In the current algorithm the integrals for estimating λ in (36) are evaluated at the element level and are projected onto the global nodes by L_2 projection. The details of this projection is described in [25]. Then (35) is solved to obtain the constrained re-distanced level set function. This step is applied after each re-distancing iteration of the level set field.

4. Numerical results and discussion

4.1. Simple advection of a cylindrical bubble

To demonstrate the ability of the algorithm, a simple test problem of advecting a cylindrical bubble through a rectangular domain was considered. The liquid is flowing with a constant uniform velocity of 1 m/s in the vertical direction. The buoyancy force is not activated. Hence the bubble should simply advect through the domain with the velocity of the liquid. The domain and the initial position of the bubble are shown in Fig. 1. The dimensions of the computational domain are $-2.0 \leqslant x \leqslant 2.0$, $-2.0 \leqslant y \leqslant 8.0$, and $0 \leqslant z \leqslant 1$ and the mesh consists of 640 hexahedral elements ($16 \times 40 \times 1$). Periodic boundary conditions are applied in x- and z-directions. A uniform velocity of 1 m/s is specified at the inlet and a constant pressure boundary condition is applied at the exit of the domain. The bubble radius is 1.25 m, and the bubble location is such that the bottom of the bubble is positioned at -1.25 m. A uniform velocity of 1 m/s and zero pressure is imposed as an initial guess throughout the domain. A step size of 0.25 s is used for the simulation, which corresponds to a Courant number of 1.0. The motion of the bubble through the domain is shown in Fig. 2. Clearly the bubble is advected with the fluid velocity of 1 m/s and also the shape of the bubble is preserved along with the conservation of the volume of the bubble. It should be noted that formulations that utilize a discontinuous scalar are unable to convect the interface without any oscillations or distortions, on such a coarse mesh.

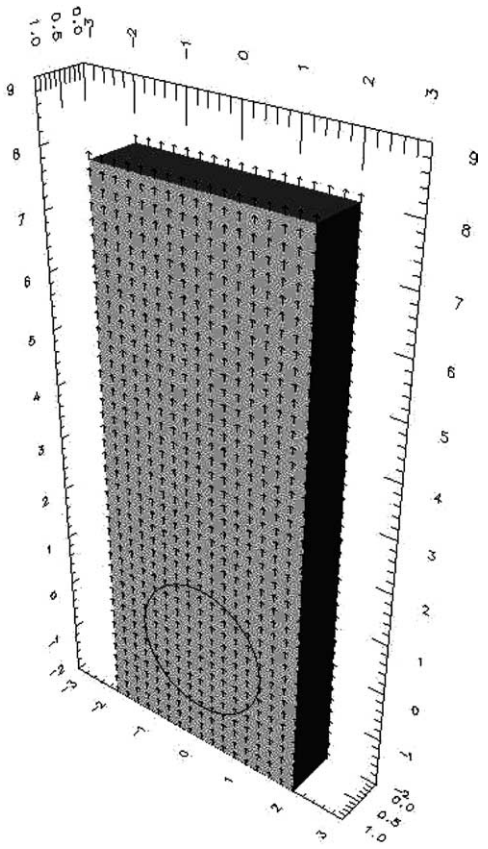

Fig. 1. The computational domain and bubble position at $t = 0$.

4.2. Two dimensional simulation of buoyant bubble motion at a medium Reynolds number

The rise and the deformation of a two dimensional gas bubble in an otherwise stationary liquid contained in a vertical, rectangular container is investigated using the level set method incorporating surface tension forces.

The density of the water and air were taken to be, 1000 kg/m^3, and 1.226 kg/m^3, respectively, which gives a density ratio of approximately 1000. The viscosity of liquid phase is taken as $3.5\,e^{-1}$ kg/m s, and the viscosity of the air to be, $3.58\,e^{-3}$ kg/m s, so that the viscosity ratio between the two phases is approximately 100. The domain width is 0.1 m and the domain length is 0.5 m. The position of the bubble is shown in Fig. 3. The initial radius of the 2-D bubble was 2.5 cm. With the above parameters, if we define the Reynolds number as, $Re = \frac{(2R_b)^{3/2}\sqrt{g}\rho_c}{\mu_c}$, and Bond Number as, $Bo = \frac{4\rho_c g R^2}{\sigma}$ then $Re = 100$, and $Bo = 200$. Grace [7] presented a diagram showing the effect of fluid properties and the equivalent bubble diameter on the shape and the terminal velocity of an isolated bubble. According to their experiments for the parameters chosen above (Eótvos number, $Eo = Bo = 200$, Morton number, $M = Bo^3/Re^4 = 0.08$), formation of a skirted bubble was reported. The mesh used in simulations consists of $100 \times 500 \times 1$ elements, and a periodic boundary condition was imposed in z direction. On the side planes, the normal component of the velocity (x-directional velocity) is specified as zero, and a zero traction was also imposed. A constant pressure boundary condition

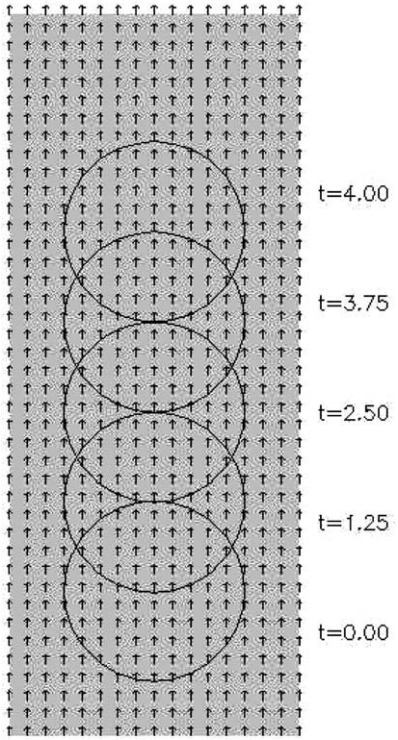

Fig. 2. Bubble position at various time instants.

was prescribed at the outflow, and a zero velocity was assigned on the bottom of the container. The initial guess for pressure is that of the hydrostatic head.

When the bubble begins to rise, due to the buoyancy force acting on the bubble, the pressure gradient at the lower surface of the bubble is higher than on the top surface. The vortex sheet which develops at the surface has a rotation (Fig. 4) which induces the motion of a jet of water that pushes into bubble from below. This phenomena is captured within the numerical simulations presented in Figs. 4 and 5. These are the solutions at the time instances of $t = 0.05$ and $t = 0.15$, respectively. At this stage, the liquid jet does not effect the liquid above the bubble. The velocity of the upper surface of the bubble in comparison to the rest of the bubble is low resulting in bubble distortion. With time, the water jet from the bottom further pushes the bubble, which, causes the lower interface to move more towards the upper cap of the bubble (Fig. 6), forming a so-called skirted bubble. Eventually the liquid jet pinches off the bubble and shreds satellite bubbles as shown in Fig. 6. This result is consistent with the findings of Delnoij et al. [28] who also observed the formation of skirted bubbles and shredding of satellite bubbles. Walter and Davidson [6] also observed the detachment of two small bubbles at the lower extremities of the main bubble, during the rise of two dimensional bubbles. The solutions obtained from this method are also in good agreement with the Sussman et al. [2], who carried out simulations at the same Reynolds and Bond number. In the simulations presented here, actual piercing of the bubble did not occur due to the relatively low Reynolds number. As seen in Fig. 6 for a low Reynolds number, the liquid jet below the bubble is not strong enough to pierce causing the bubble instead to rise as a cap. Due to the redistancing strategy adopted, the level sets remains a distance function despite the change in bubble topology. The advantage of the levels sets is also demonstrated as the shredded bubble's motion was predicted without altering the algorithm. However, resolving the shredded bubbles completely requires much higher resolution, thus the interest in future work on adaptivity.

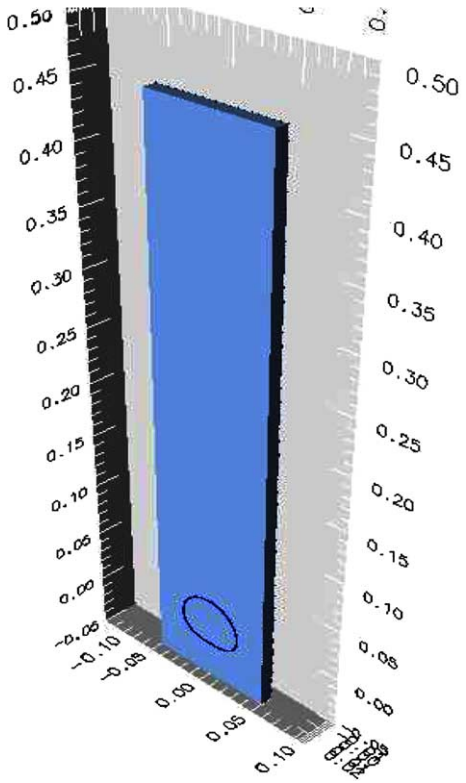

Fig. 3. The bubble position at $t = 0$.

4.3. Effect of fluid viscosity on buoyant spherical bubble motion

To further demonstrate the capability of the algorithm, a three-dimensional simulation of the motion of the bubble was performed. Starting from a perfectly spherical 3-D bubble which was initially at rest, buoyancy induced motion of the bubble is studied by tracking the interface using the level set method. The fluid viscosity plays an important role in determining the involved bubble dynamics, thus manifesting the change in the shape of the bubble. Hence the effect of Reynolds number on the bubble motion is an interesting phenomena to study. We consider two cases, one with a low Reynolds number of 10, and the other case with $Re = 100$.

For the three dimensional simulations presented in this section, the domain is a rectangular box with a length of 6.48 m, and the width and thickness of the box is 2.07 m. The calculations are performed on a $50 \times 150 \times 50$ hexahedral elements mesh. Initially the bubble of 0.5 m radius is positioned at 0.7 m from the bottom of the box. The initial position of the bubble is shown in the Fig. 7(a). All of the surfaces are modeled as slip walls. Initially the fluid is at rest, hence a zero velocity is imposed throughout the domain, where as pressure is initialized to that of the hydrostatic head.

4.3.1. Formation of a cap bubble at low Reynolds number

To investigate the viscous effects on the bubble motion, a Reynolds number of 10 and a Bond number of 5 is chosen. The ratio of density of the liquid to gas is 40, and the ratio of the viscosities is also chosen as 40. From the parameters it is clear that this is a flow with high viscosity and surface tension. Again, the results

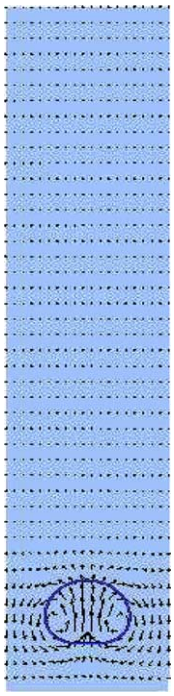

Fig. 4. Evolution of rising buoyant bubble at $t = 0.05$.

are in good agreement with the experimental findings of Grace [7]. For the chosen parameters ($Eo = 5$, $M = 0.0125$), the experiments resulted in the formation of a spherical cap bubble.

Fig. 7 presents the bubble shape at different time instants obtained from simulations. Initially, the bubble rises to form an elliptical shape bubble as shown in Fig. 7(b) ($t = 0.0625$ s) due to the pressure gradient between the upper and the lower surfaces of the bubble. The bottom view at the same time instant (Fig. 7(c)) shows the slight roll up of the lower surface. As the time progress, the liquid jet below the bubble pushesthe lower surface further as shown in Fig. 7(d) and (e). Fig. 8(a) presents the contours of the vertical velocity at time $t = 1.25$ s on a xy-plane through the center of the domain. As seen in the figure, the upper surface travels faster than the lower and also, the bottom surface gets much flatter giving the bubble a spherical cap shape 7. Further in time, as shown in Figs. 7(f,g) and 8(b), the upper surface deforms more into the cap, as the tip of the top surface travels fast compared to the rest of the bubble. The jet from the bottom is not strong enough, and hence gets decelerated due to the viscous and surface tension forces as shown in Fig. 8(c). Also from the figure we can see that the jet speed is more diffused and hence making the bubble to broaden slightly. The bubble then continues to rise as spherical cap bubble (Figs. 7(h), 8(d)).

4.3.2. Formation of a toroidal bubble at high Reynolds number

In this section, we consider a high Reynolds number of 100, and a Bond number of 50 (compared to Section 4.3.1) to study how the bubble shape can be affected by varying (decreasing in this case) the viscous and surface tension effects. Both the density and the viscosity ratios are chosen to be 80 (similar to the parameters presented in [22]). The initial conditions are similar to that of in Section 4.3.1. Fig. 9 presents the shape of the bubble at various time instants, and Fig. 10 display the bubble interface on a xy-plane cut through the domain, along with the velocity vectors.

As described earlier the liquid jet from the bottom tries to push the lower surface of the bubble (Fig. 10(a)), which can also be seen in Fig. 10(b). The deformation of the bubble from sphere to elliptic cap

Fig. 5. Evolution of rising buoyant bubble at $t = 0.15$.

Fig. 6. Evolution of rising buoyant bubble at $t = 0.3$.

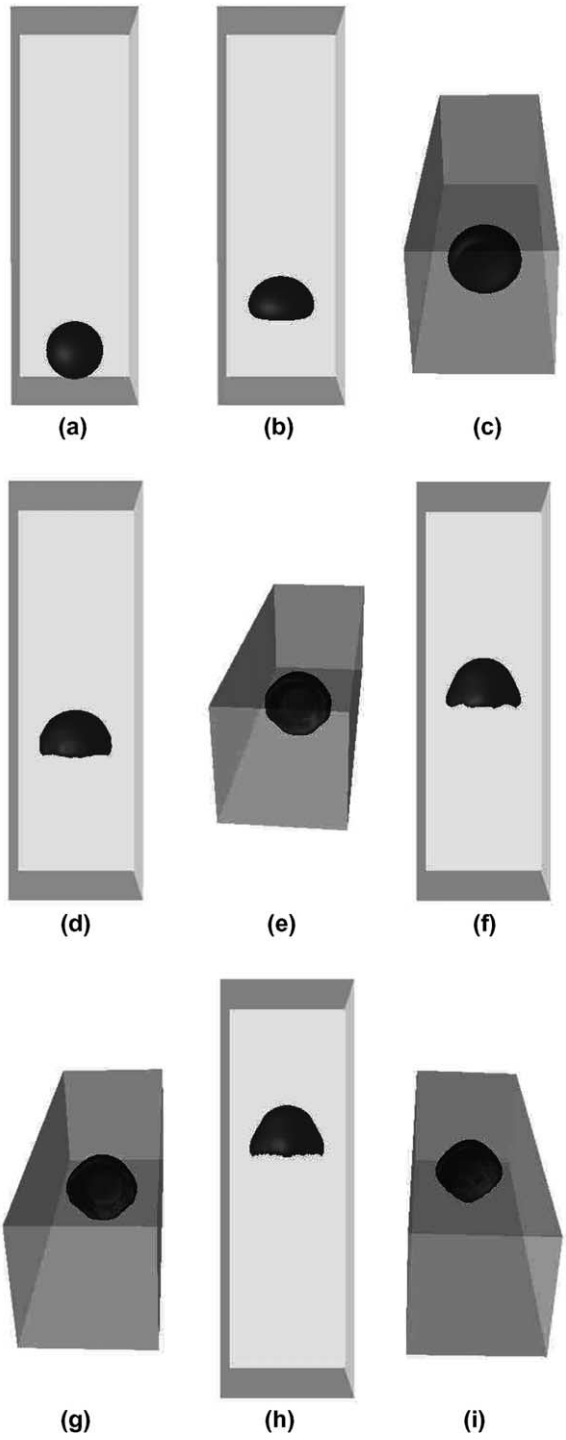

Fig. 7. Rise of the spherical bubble at low Reynolds number: (a) $t = 0$, (b,c) $t = 0.625$, (d,e) $t = 1.25$, (f,g) $t = 1.875$, (h,i) $t = 2.5$.

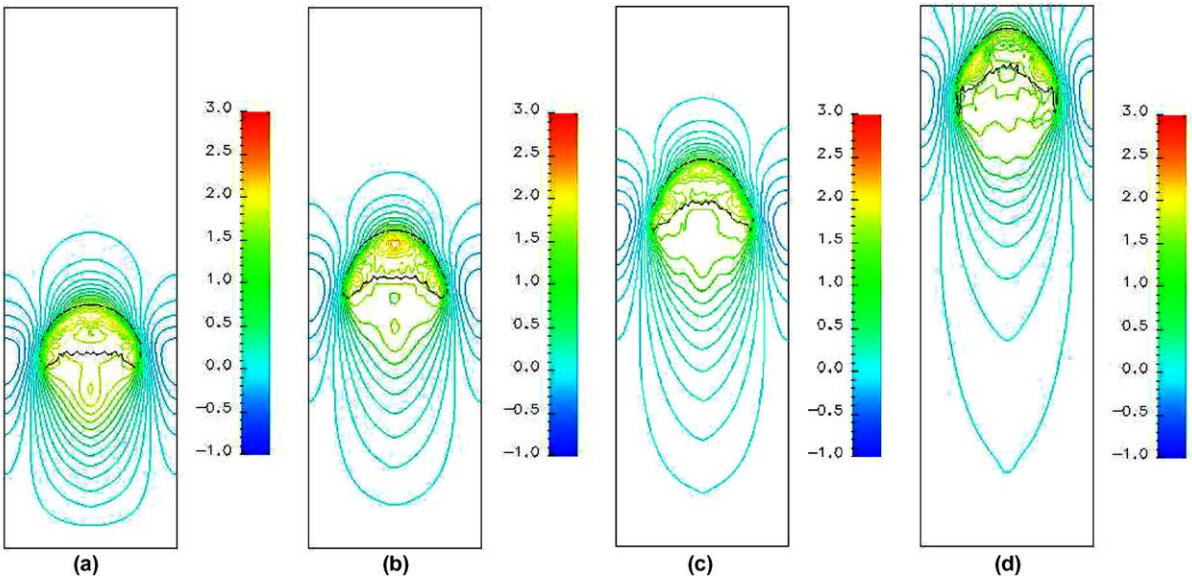

Fig. 8. Vertical velocity contours shown on the *xy*-plane (low Re): (a) $t = 1.25$, (b) $t = 1.875$, (c) $t = 2.5$, (d) $t = 3.75$.

due to the jet can be seen in Fig. 9(b). As the time progress the jet gets much stronger, and rolls the bottom interface further as seen in Figs. 9(d) and 10(c). Fig. 9(e) shows the further deformation of the bubble at $t = 0.5$ s. At this instant of time the impinging jet from the bottom can be seen in Fig. 10(d). As the velocity along the axis of the bubble is higher as compared to the rest, and also the top surface of the bubble traveling faster, the bubble assumes a bell shape (Fig. 9(e)). We can see from the Fig. 9(e) that, although the liquid pushes the bottom surface closer to the top, it does not yet pierce the top surface. Further in time at $t = 0.625$ s, the jet finally pierces the top surface and detaches it from the rest of the bubble. This can be seen in Fig. 9(f). The bottom view of the same presented in Fig. 9(g) shows clearly the part of the interface detaching from the rest of the bubble. This can also be seen in the two dimensional view presented in Fig. 10(e). Eventually at time $t = 0.75$ s, the jet penetrates the liquid bubble and lower surface pierces the top surface completely, which can be seen clearly in Fig. 9(f). Thus the formation of a toroidal bubble is complete as seen from the bottom view of the bubble in Fig. 9(f). The vorticity in the bubble surface is transferred to circulation about this annular toroidal bubble (Fig. 10(e)). The observations made in this section are in good agreement with the features of three dimensional bubbles reported from the experiments of Walters et al. [6]. Similar numerical results were reported by Li et al. [22].

4.4. Three dimensional simulation of two bubble coalescence

To demonstrate the capability of the algorithm in computing interface singularities such as merging and reconnection, we consider the interaction of two bubbles of the same density under the influence of a buoyancy force. The domain is a unit cube, and the initial position of the bubbles is shown in Fig. 11. The upper bubble is of radius 0.15 and is centered at (0.5, 0.6). The lower bubble is centered at (0.5, 0.35) with a radius of 0.1. The non-dimensional fluid density inside the bubbles is 1.0, where as the fluid density outside the bubbles is 10.0. The viscosity of the fluid inside the two bubbles is 0.00025, and the viscosity of the fluid outside the bubbles is 0.0005. The effect of surface tension was not considered here. Initially the fluid is at rest. Periodic boundary conditions are applied in all the three directions. A gravitational force is applied in the vertically downward direction. The body force was adjusted such that the net momentum flux

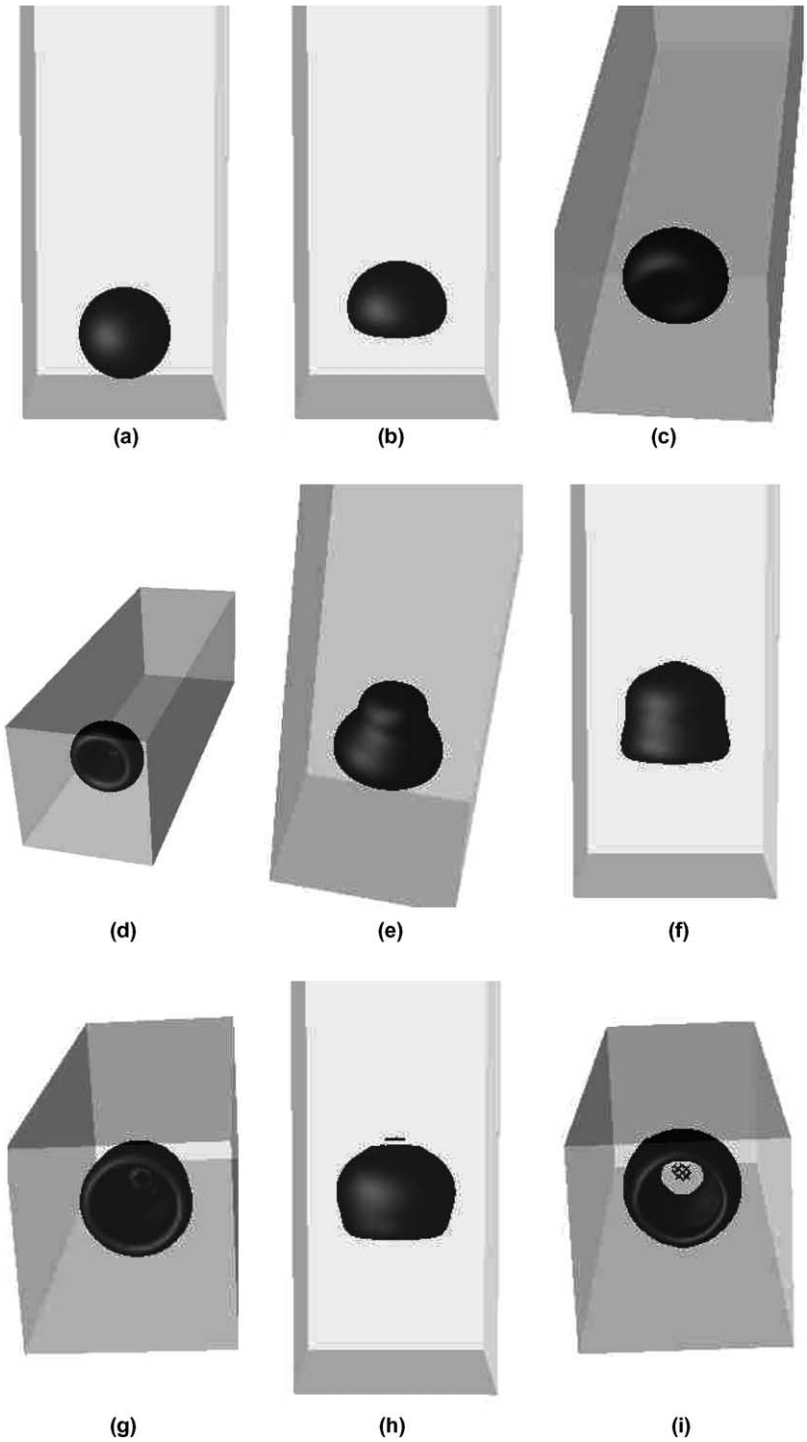

Fig. 9. Rise of the spherical bubble at high Reynolds number: (a) $t = 0$; (b,c) $t = 0.25$, (d) $t = 0.375$, (e) $t = 0.5$, (f,g) $t = 0.625$, (h,i) $t = 0.75$.

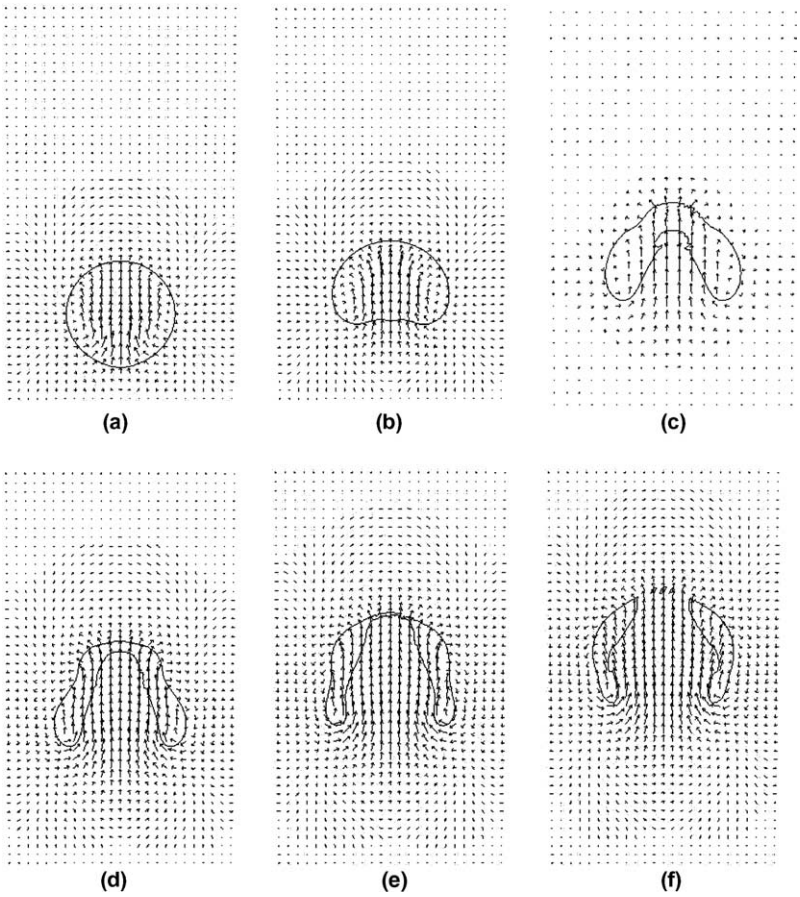

Fig. 10. Change in the shape of the interface displayed on a xy-plane along with velocity vectors: (a) $t = 0.125$, (b) $t = 0.25$, (c) $t = 0.375$, (d) $t = 0.5$, (e) $t = 0.625$, (f) $t = 0.75$.

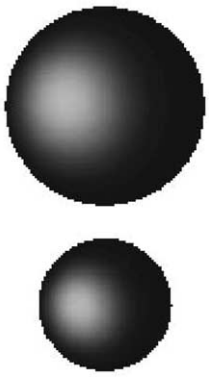

Fig. 11. Initial position of the bubbles.

through the boundaries of the domain was zero. In order to achieve this, an additional force term defined by $\rho_0 g$, was subtracted from the original body force term, where $\rho_0 = \alpha\rho_b + (1-\alpha)\rho_f$ is the mean density, and $\alpha = \sum_{i=1}^{N_b} \pi d_i^3 / 6L^3$ is the void fraction, N_b is the number of bubbles (here $N_b = 2$) and d_i is the diameter of the ith bubble, and L is the length of the cubic domain. This additional term prevents the uniform vertical acceleration of the whole flow field and allows for periodic boundary conditions to be used. This term is analogous to the pressure gradient generated by the base of the container, which balances the total gravitational force on the fluid. We have chosen a uniform mesh of $80 \times 80 \times 80$ hexahedral elements.

As the bubbles are lighter than the surrounding fluid, they will rise with time. Fig. 12 shows the position of the bubbles at $t = 0.05$, the dimensionless time. Fig. 13 displays the contours of speed at which the bubbles travel on a xy-plane cut through the center of the domain. We can see from the figure that the bottom interface of the bubbles travels faster compared to the front. However the second bubble, which is in the wake of the larger bubble, tries to move fast from the front too. As the time evolves, the upward moving jet produced by the lower bubble not only affects the larger bubble transients, but also dictates the shape of the smaller bubble as shown in the Fig. 14. This jet creates opposite signed vorticity fields in the wake of the large bubble as shown in Fig. 15. From the pressure contours displayed on a xy-plane (at time $t = 0.10$), one can observe that the lower pressure field behind the large bubble causes a strong flow on the bottom portion

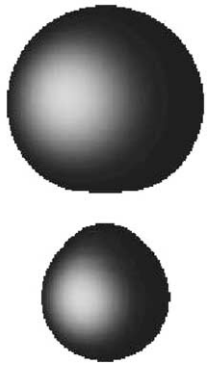

Fig. 12. Position of the bubbles at $t = 0.05$.

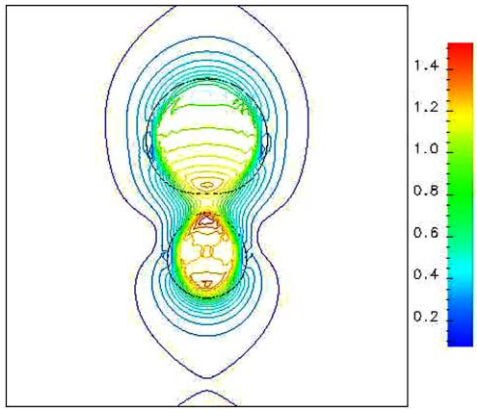

Fig. 13. Contours of speed on a cut plane at $t = 0.05$.

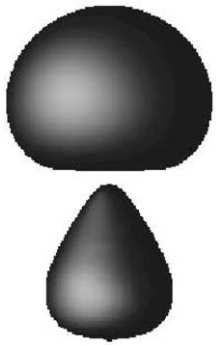

Fig. 14. Position of the bubbles at $t = 0.10$.

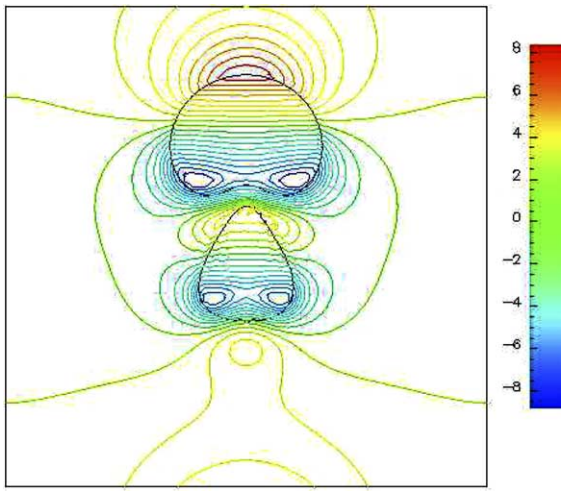

Fig. 15. Position of the bubbles at $t = 0.10$ along with the contours of pressure on a cut plane.

Fig. 16. About to merge bubbles at $t = 0.15$.

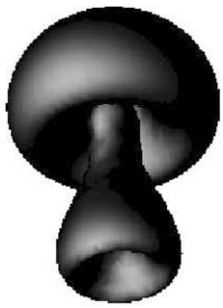

Fig. 17. A different view of the bubbles which are about to merge at $t = 0.15$.

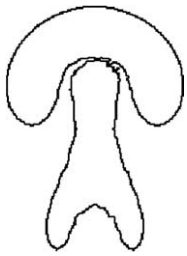

Fig. 18. The interface of about to merge bubbles on a cut plane at $t = 0.15$.

Fig. 19. Merged bubbles at $t = 0.22$.

of the large bubble and as well affecting the front portion of the smaller bubble following the larger bubble. One can see a similar wake at the bottom of the smaller bubble too. Figs. 14 and 15 clearly shows also the narrowing of the smaller bubble in the process. At time $t = 0.15$ (Fig. 16), the front portion of the small bubble almost catches up with the bottom portion of the larger bubble. Also the vorticity created at the bottom of the larger bubble causes the bubble to roll up as shown in Fig. 17. The incipient merging of the interfaces is seen more clearly in Fig. 18, in which a plane (xy) is cut through the domain. Fig. 19 shows the merged bubbles at $t = 0.27$. Fig. 20 depicts the interfaces on a plane clearly showing the merged interfaces and also some of the entrained heavier fluid inside the incident new bubble.

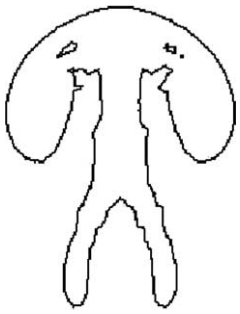

Fig. 20. The interface of merged bubbles on a cut plane at $t = 0.22$.

5. Conclusions

In summary, we have applied the stabilized finite element formulation along with the level set method to evaluate two-phase incompressible flows in two and three dimensions. The formulation derived is purely Eulerian, and no explicit tracking of the interface is required. The interface is readily obtained by locating the zero level set of the level set field. The robustness of the method to compute the flows with the large density and viscosity differences is demonstrated. The surfaces tension forces were also accounted for in the simulations. The re-distancing strategy allows the distance field to be maintained and assures mass conservation. The two- and the three- dimensional results clearly show the ability of the method to handle the bubble coalescence and breakup. The future work should focus on extracting the advantage of FEM by evaluating two-phase flows in complex geometries with the an efficient adaptive meshing strategy. The simulations presented in Section 4.4 will certainly benefit from adaptive remeshing to resolve the merging interfaces more efficiently.

Acknowledgement

The authors wish to acknowledge the support given to this study by a USDOE-NEER grant, DOE-FG02-99ID13776. This work was partially supported by National Computational Science Alliance under MCA01S014N and utilized both the Silicon Graphics Origin 2000 system and the IA-64 Linux cluster.

References

[1] J.A. Sethian, Level Set Methods and Fast Marching Methods, Cambridge University Press, 1999.
[2] M. Sussman, P. Smereka, S.J. Oshe, A level set approach for computing solutions to incompressible two-phase flows, J. Comput. Phys. 114 (1994) 146.
[3] M. Sussman, A.S. Almgren, J.B. Bell, L.H. Howell, P. Colella, W.L. Welcome, An adaptive level set approach for incompressible two-phase flows, J. Comput. Phys. 148 (1999) 81–124.
[4] J.U. Brackbill, D.B. Kothe, C. Zemach, A continuum method for modeling surface tension, J. Comput. Phys. 100 (1992) 335–354.
[5] R.A. Hartunian, W.R. Sears, On the instability of small gas bubbles moving uniformly in various liquids, J. Fluid Mech. 3 (1957) 27–47.
[6] J.K. Walters, J.F. Davidson, The initial motion of a gas bubble formed in an inviscid liquid. Part-2. The three dimensional bubble and the toroidal bubble, J. Fluid Mech. 17 (1963) 321–336.
[7] J.R. Grace, Shapes and velocities of bubbles rising in infiite liquids, Trans. Inst. Chem. Engrg. 51 (1973) 116–120.
[8] D. Bhaga, M.E. Weber, Bubbles in viscous liquids: shapes, wakes, and velocities, J. Fluid Mech. 105 (1981) 61–85.
[9] A.N. Brooks, T.J.R. Hughes, Streamline upwind/Petrov–Galerkin formulations for convection dominated flows with particular emphasis on the incompressible Navier–Stokes equations, Comput. Methods Appl. Mech. Engrg. 32 (1982) 199–259.

[10] T.J.R. Hughes, L.P. Franca, G.M. Hulbert, A new finite element formulation for fluid dynamics: VIII. The Galerkin/least-squares method for advective–diffusive equations, Comput. Methods Appl. Mech. Engrg. 73 (1989) 173–189.
[11] T.J.R. Hughes, Multiscale phenomena: Green's functions, the Dirichlet-to-Neumann formulation, subgrid scale models, bubbles and the origins of stabilized methods, Comput. Methods Appl. Mech. Engrg. 127 (1995) 387–401.
[12] A. Rússo, Bubble stabilization of the finite element methods for the linearized incompressible Navier–Stokes equations, Comput. Methods. Appl. Mech. Engrg. 132 (1996) 335–343.
[13] F. Brezzi, L.P. Franca, T.J.R. Hughes, A. Russo, $b = \int g$, Comput. Methods Appl. Mech. Engrg. 145 (1997) 329–339.
[14] L.P. Franca, S. Frey, Stabilized finite element methods: II. The incompressible Navier–Stokes equations, Comput. Methods Appl. Mech. Engrg. 99 (1992) 209–233.
[15] T.E. Tezduyar, Finite element methods for flow problems with moving boundaries and interfaces, Arch. Comput. Methods Engrg. 8 (2001) 83–130.
[16] S.O. Unverdi, G. Tryggvason, A front tracking method for viscous, incompressible, multifluid flows, J. Comput. Phys. 100 (1992) 25.
[17] J.P. Best, The formation of toroidal bubbles upon the collapse of transient cavities, J. Fluid Mech. 251 (1993) 79.
[18] T.J.R. Hughes, W.K. Liu, T.K. Zimmermann, Lagrangian–Eulerian finite element element formulation for incompressible viscous flows, Comput. Methods Appl. Mech. Engrg. 29 (1981) 329–349.
[19] T.E. Tezduyar, M. Behr, J. Liou, A new strategy for finite element computations involving moving boundaries and interfaces. The deforming-spatial-domain/space-time procedure: I. The concept and the preliminary numerical tests,, Comput. Methods Appl. Mech. Engrg. 94 (1992) 339–351.
[20] T.E. Tezduyar, M. Behr, S. Mittal, J. Liou, A new strategy for finite element computations involving moving boundaries and interfaces. The deforming-spatial-domain/space-time procedure. II. Computation of free-surface flows, two-liquid flows, and flows with drifting cylinders, Comput. Methods Appl. Mech. Engrg. 94 (1992) 353–371.
[21] C.W. Hirt, B.D. Nichols, Volume of fluid (VOF) method for the dynamics of free boundaries, J. Comput. Phys. 39 (1981) 201.
[22] C. Li, S.V. Garimalla, J.A. Reizes, E. Leonardi, The development of a bubble rising in a viscous liquid, J. Fluid Mech. 387 (1999) 61–96.
[23] T. Barth, J.A. Sethian, Numerical schemes for the Hamilton–Jacobi and level set equations on triangulated domains, J. Comput. Phys. 145 (1998) 1–40.
[24] C.H. Whiting, K.E. Jansen, A stabilized finite element method for the incompressible Navier–Stokes equations using a hierarchical basis, Int. J. Numer. Methods Fluids 35 (2001) 93–116.
[25] K.E. Jansen, S.S. Collis, C.H. Whiting, F. Shakib, A better consistency for low-order stabilized finite element methods, Comput. Methods Appl. Mech. Engrg. 174 (1999) 153–170.
[26] Y.C. Chang, T.Y. Hou, B. Merriman, S. Osher, Eulerian capturing methods based on a level set formulation for incompressible fluid interfaces, J. Comput. Phys. 124 (1996) 449.
[27] C.A. Taylor, T.J.R. Hughes, C.K. Zarins, Finite element modeling of blood flow in arteries, Comput. Methods Appl. Mech. Engrg. 158 (1998) 155–196.
[28] E. Delnoij, J.A.M. Kuipers, W.P.M. van Swaaij, Computational fluid dynamics applied to gas-liquid contactors, Chem. Engrg. Sci. 52 (21/22) (1997) 3623.